INTERNATIONAL JOURNAL OF PRECISION ENGINEERING AND MANUFACTURING Vol. 19, No. 3, pp. 431-439 MARCH 2018 / 431

REGULAR PAPER

DOI: 10.1007/s12541-018-0052-9
ISSN 2234-7593 (Print) / 2005-4602 (Online)

Evaluations of Surface Integrity and Mechanical Performance in Laser Melting of Stainless Steel Powders with Heterogeneous Metal Substrates

Chunliang Kuo[1,#], Weijun Peng[1], and Anchun Chiang[1]

1 School of Mechanical Engineering, National Taiwan University of Science and Technology, 43 Keelung road, Sec. 4 Taipei, 10607, Taiwan
Corresponding Author / E-mail: chunliang.kuo@mail.ntust.edu.tw, TEL: +886-2-2733-3141 (ext. 6448)
ORCID: 0000-0002-7271-2627

KEYWORDS: Laser melting powder, Heterogeneous substrate, Elemental migration, Microstructure, Microhardness, Ultimate tensile strength

This paper outlines advances in the processing technology of layer manufacturing in conjunction with laser melting metallic powders (stainless steel 316L) on heterogeneous metal substrates (stainless steel 316). Elemental migration of chromium and nickel in the fusion/dilution zone which led to possible strengthening mechanisms was analysed. Two-phase austenitic microstructures in the body were found to dilute into the stainless steel 316 substrate matrixes leading to the strengthening in the conjunction. Laser power was shown to be particularly significant (F_{cal}: 6.03, PCR: 47.9%) to produce high microhardness (~268 $HV_{0.1}$) depending on the increase in ferrite content. In the confirmation runs, high tensile strength was achieved (834 MPa) with high density (7.64 g/cm^3) due to the smoothened elemental migration of chrome and nickel, the strengthened matrix in the duplex structure, and the enhanced microhardness under the input high energy density.

Manuscript received: July 3, 2017 / Revised: September 3, 2017 / Accepted: November 20, 2017

1. Introduction

Layered manufacturing represents a pronounced shift towards rapid manufacturing from prototyping, driven by the need for shortened tooling lead times and increased production runs, as reported by Wohlers.[1] Many of the important developments in the layered manufacturing of polymers, such as hybrid-3D printing (3DP)[2] and fused deposition modelling (FDM)[3], are being applied to metallic materials. Metal additive manufacturing is among the most promising alternatives to conventional machining, and has already been applied in the large-scale production of bicycle components[4], aerospace parts[5] and rapid prototyping tools.[6]

According to Das[7], he demonstrated that epitaxial solidification can break through the impurity/oxide films and produce intimate bonds between grains and the partially melted substrate, as long as the operating temperature reaches the melting point of the powder. When provided with thermal energy sufficient to enable dilution and the growth of grains at the interface between the melted substrate and solidified powder, the resulting dense material delivers high mechanical integrity. Fischer et al.[8] reported that in the time domain, the absorption and diffusion of energy (in terms of penetration depth) could be less than the radius of the particles (20-30 μm) within an interaction time of 0.1-1 μs. A pulse interval of less than 1 μs was shown to limit the depth of thermal penetration to less than 10 μm in Ni, Stellite 6, and Ti powders, which is the average radius of the particles used in selective laser sintering. Rombouts et al.[9] reported that contamination (oxide, impurities) can reduce the surface energy, thereby limiting wetting and spreading and leading to lower surface free energy in the selective laser sintering process. This can be attributed to the fact that metal oxides have a lower solid-vapour surface free energy (compared to the corresponding liquid-vapour surface free energy), which produces a negative spreading coefficient. As a result, the molten alloy undergoes balling, which minimises the contact area and leads to poor consolidation.

Following the interpreting of the physics behind the laser energy event, the interaction of the alloying elements coupled with the operating parameters in the proper combination could also effectively influence the outcomes. Kruth et al.[10] suggested that ferrous powder alloyed using phosphorous could reduce the melting temperature and surface tension, thereby preventing balling effects and enhancing surface quality. They reported that under the appropriate operating parameters, a suitable composition (Ni: 20%, Cu: 15%, Fe_3P: 15%) and powder morphology (irregular grain shape) could achieve a maximum

mechanical strength of 395 MPa, average microhardness of 220 $HV_{0.22}$, and surface roughness of only Ra 17 μm. Gu and Shen[11] classified two distinct phenomena: shrinkage-induced balling and self-balling resulting from direct metal laser sintering of stainless steel powder. They also suggested that a deoxidising agent (H_3BO_3 and KBF_4) could be used to suppress the formation of oxidation films; and thereby promote spreading and subsequent consolidation. Jaroslav Čapek et al.[12] studied the microstructure and mechanical behaviour in the porous (87 vol. %) scaffold prepared by SLM of SST316L under laser power (200 W), scanning rate (200 mm/s) and hatch space (1 mm). They reported that the rapid cooling in SLM could produce a strengthening phase such as cellular dendritic microstructure, with tensile strength of 3.46±0.25 MPa suitable for implantation of trabecular bone. Khademzadeh et al.[13] investigated the influence of the prepared powder mixtures of commercially pure Ti (D_{50}=300 μm) and Ni (D_{50}=50 μm) for metal deposition using micro-laser sintering. They found that the alloyed powder mixtures could easily produce NiTi single phase with a sustainable NiTi microstructure, since the internal energy of the milled powder particles was beneficially added to the input energy from the laser deposition.

Mechanical performance can be improved conventionally by the optimisation of the operating parameters or scanning strategies for the metallurgical alteration, leading to an enhancement of the microstructure. Tolosa et al.[14] reported that the fabrication of parts via layering over the X-Y plane with growth along the Z-axis results in material with tensile strength (528-557 MPa) below that of wrought material (520-680 MPa) due to the discontinuous bonds layered in the Z-axis. Nonetheless, the hardness (235 HV) achieved in that study was homogeneous and at a level similar to that of wrought material, regardless of orientation and inclination between layers. Choi et al.[15] investigated the influence of single pulse irradiation (75.53-527.88 mJ/cm^2) and scanning speed (10-70 μm/s) in laser-induced line structuring on stainless steel. The results showed that when operated in the higher irradiation (527.88 mJ/cm^2) with a combination of the lower scanning speed, the formation of the laser-induced nano-scale structures could be produced. On the other hand, Wei et al.[16] presented parametric optimization for strengthening in the matrix when employing laser power of 110 W, scanning speed of 350 m/s and scanning spacing of 0.08 mm in SLM of the powder mixtures of nHA and SST316. They concluded that the decreasing scanning speed led to the increase in laser energy density, and whereby enhanced the tensile strength (~612.7 MPa) and the microhardness (~246.2 HV). Sun et al.[17] reported when employing parameters of laser power of 380W, scanning speed of 3000 mm/s and hatch spacing of 25 μm in SLM of SST316L powders, it could greatly increase the microhardness (~220 HV), compared to the standard annealed counterpart of ~155 HV. This can be attributed to the increased dislocation density, nanoscale amorphous inclusions and the formation of the two phases (primary γFCC and retained δBCC) in the matrix.

While parametric optimisation could result in the appreciable mechanical performance, the use of the powder mixtures could activate the production of a composite microstructure which greatly strengthened the mechanical performance. Hao et al.[18] presented parametric optimization for strengthening in the matrix when employing laser power of 42.2 W, scanning speed of 0.160 m/s and scanning spacing of 50 μm in SLM of powder mixtures of hydroxyapatite (HA) and 316 stainless steel (SST). They concluded that the duplicate scanning strategy produced heterogeneous nucleation in fine grain of 316SS/HA, whereby enhancing the tensile strength (~95 MPa) and high microhardness (~241.4 HV). AlMangour et al.[19] presented that the TiB2/SST316L nanocomposites could be fabricated in SLM under the laser power of 100 W, hatch spacing of 0.12 mm, scanning speeds of 83.3 mm/s. The incorporating TiB2 reinforcements (15 vol. %) in the SST316L matrix could form the nanoscale structure which greatly enhanced the microhardness (611 $HV_{0.1}$), compared to the unreinforced SST316L (210-233 $HV_{0.1}$). On the other hand, the applied laser energies in a hybrid form could alter the heating and cooling effects in the melting pool during solidification. Hence, the mechanical performance could be greatly optimised. Joo et al.[20] investigated the performance of hardness using hybrid CO2 laser-GMA welding for the dissimilar materials such as the AH32 workpiece joining on the stainless steel (SST304L) substrate. The tests were operated by the Taguchi (L_{18}) method with welding speed 1.3-1.5 m/min, welding current 230-300 A, laser-arc distance 0-4 mm and welding voltage 23-27 V. The results show that the hardness at a distance of 3 mm over the bottom surface (297 HV) was higher than that at distance of 12 mm over the bottom surface (195 HV). This strengthening effect is due to the lower part being affected mainly by rapid heating and cooling during the laser process.

Conventional powder bed-based additive manufacturing methods can be used to layer geometrical features through the transformation of the homogeneous powder graining the high mechanical performance and complete surface integrity. Table 1 lists the survey reflecting the state-of-the-art laser meting and their corresponding results obtained from the associated parametric optimisations. In contrast, this newly developed printing process fabricates features from existing heterogeneous metal plates. This paper investigates the effects of coordinating scanning speeds with the spacing and thickness of layers in order to maximise mechanical performance in heterogeneous metal devices without compromising surface integrity. The operating parameters were varied as follows: laser power (100-200 W), exposure (50-175 μs), and point distance (35-70 μm) based on calculated energy densities for melting. Our aim was to identify the parameters capable of optimising tensile strength, density, and microhardness, and microstructure. The characteristics of micro-hardness and microstructure at the interfaces within layered bodies and heterogeneous substrates were also investigated in detail.

2. Experiment Procedure and Data Collection

2.1 Powder material, laser source, scanning strategy, and machine tool set-up

All testing was performed at the additive manufacturing centre (Renishaw AM250, UK) using a SPI Ytterbium fibre laser having a wavelength of 1070 nm with a maximum laser power of 200 W and laser spot 75 μm on the bed. Fig. 1(a) shows the schematics for the printing process which was performed on the heterogeneous metal substrate (AISI 316, thickness: 0.87 mm), with layering metallic powders of SST316L for building up the mechanical features. Table 2 lists the chemical composition obtained from the AISI 316 stainless steel plate and 316L stainless steel powders used in the experiments; whereas in Table 3 the mechanical properties are listed for further discussion. The

Table 1 A survey for elemental migration, microhardness and microstructure in laser melting of SST 316L

Literature source	Laser molten powder	Laser power (W)	Exposure duration (μs)	Scanning point distance (μm)	Energy density (W/mm^3)	Elemental migration	Hardness (MPa)	Microstructure
Chen et al.[21]	5Cr-Ni-4Mo	77.5	75-150	50	129-258	Dispersion of Cr, Ni, C	N/A	heterogeneous martensitic structure
Zhu et al.[22]	SST 316L	200	100	110	N/A	N/A	2700	2-3 μm austenitic grains
Sander et al.[23]	SST 316L	165-285	34-47	110	39-75	N/A	N/A	uniform austenitic structure
Suryawanshi et al.[24]	SST 316L	90	30	150	20	N/A	N/A	30-80 μm FCC austenitic grains
Cherry et al.[25]	SST 316L	180	75-125	25-75	42-209	No disintegrated element being observed	225	N/A
Wang et al.[26]	SST 304L	2300-4000	189-235	2500	N/A	N/A	N/A	δ-ferrite dendrites inside austenite matrix

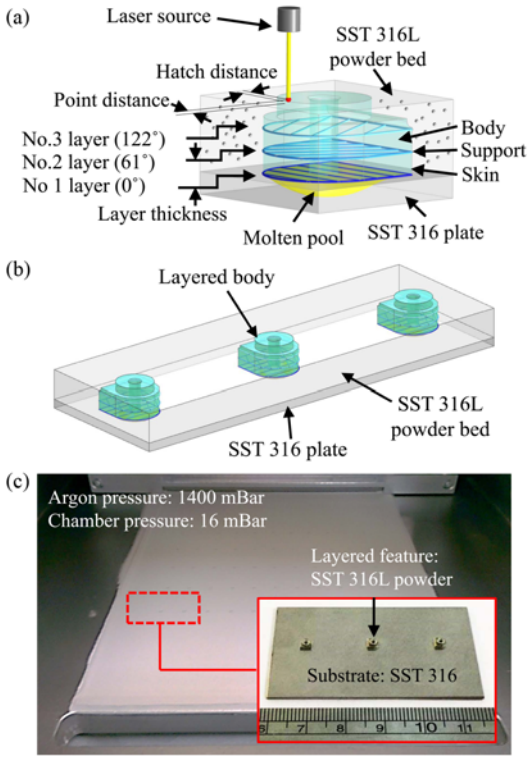

Fig. 1 Schematics of the (a) scanning strategy, (b) layered mechanical features, and (c) machine set-up for laser melting of metallic powers on homogenous substrate

particles in the stainless steel powder ranged in size from 25 μm to 35 μm, having a melting point of 1371-1399ºC. The three-dimensional printing was performed using an ytterbium fibre laser (wavelength: 1070 nm) operated in the modulated mode with good control of the repetition rate. The build rate was estimated at 5-20 cm^3, depending on the scanning speed and thickness of the layers, when using a powder with an average particle size of ~45 μm. Fig. 1(b) illustrates the scanning strategy used in this study, in which the scanning orientation was rotated 61º clockwise prior to the application of each of the 45 successive layers. Scanning speed was varied according to the function of the printed skin, support and body in the layer. The inter-layer support or fillers to build up the body were fed at a moderate speed of 220 mm/s, whereas the exterior skin was printed at a relatively low speed of 700 mm/s. Fig. 1(c) shows the machine set-up and the printed geometrical features of melting SST316L powders in conjunction with the AISI 316 plate in a volume production scale.

Table 2 Composition of stainless steel used in substrate and powder

Component properties	AISI 316 (substrate)	316L SLM (powder mixtures)
Chromium	10-20%	16-18%
Nickel	1-10%	10-14%
Copper	-	0.5-1%
Manganese	0.5-1%	≤2%
Molybdenum	-	2-3%
Silicon	≤0.075%	<1%
Carbon	0.08%	0.03%
Iron	Balance	Balance

Table 3 Properties of laser melted stainless steel 316L

Mechanical data	AISI 316	SST316L
Tensile strength (UTS), MPa	580	588-683
Elongation at break (%)	50	46-54
Hardness, HV0.5	151	224-244

2.2 Experimental design

Three-dimensional printing was conducted using selective laser melting (SLM) with the parameters listed in Table 4. The parametric combinations of critical variables, such as laser power, exposure, and point distance were investigated in order to identify the optimal configuration with regard to the effects of chemical alloying, metallurgical strengthening, preferable microstructure, microhardness and ultimate tensile strength. Based on the calculated energy densities (E), these investigations and optimisation were therefore achieved in an efficient manner using the Taguchi L_9 test array as shown in Table 5, in conjunction with analysis of variance (ANOVA) for the examination of the significance in the operating parameters. In Eqs (1)-(3), the calculated volumetric energy densities were the key indicators with respect to the heat input to the melting pool in the laser process, which affected the consolidation process in a macro aspect. Whereas the combinations of the operating parameters varied the effects of the elemental migration in the alloying process, strengthening in the microstructure, and alteration of the microhardness. Thus, the final validation runs are needed to confirm the mechanical performance based

Table 4 Fixed process parameters

Factor	SS 316L SLM powder
Powder particle size, (μm)	25-35 (90%)
Scanning speed (skin), (mm/s)	700
Scanning speed (body), (mm/s)	220
Scanning speed (support), (mm/s)	220
Laser beam spot size, (μm)	75
Layers thickness, (μm)	30
Scanning spacing, (μm)	125
Number of layers	45

Table 5 Taguchi L_9 test array for 3D printing of SS 316L

Test No.	Laser power (W)	Exposure (μs)	Point distance (μm)	Calculated volumetric energy density (W/mm^3)
1	100	50	35	761,905
2	100	75	52	512,821
3	100	100	70	380,952
4	150	50	52	769,231
5	150	75	70	571,429
6	150	100	35	1,142,857
7	200	50	70	761,905
8	200	75	35	1,523,810
9	200	100	52	1,025,641

on the operating parametric combinations.

2.3 Data collection

The density of the material was measured using the Archimedes' method in ethanol with changes in level detected using a Keyence LK-H025 laser sensor at an acquisition rate of 5 kHz. Element analysis was conducted using an energy-dispersive X-ray spectroscopy system (Inca EDX). The evaluated zones were from the longitudinal section across the neutral plane, including the body and underlying substrate. The subsurface microstructure was observed via scanning electron microscopy (Jeol 6390LV), capable of reducing to a spot size of 3 nm with magnification reaching 100,000×. Microhardness measurements were similarly obtained from longitudinal and transverse sections across the sectioned plane, mapping to the same measuring points in the elemental analysis, as shown in Figs. 2(a) and 2(b), respectively. The average microhardness was from three measurements obtained from three different paths using a Vickers indentation device (Mitutoyo MVK-H1) with a load of 100 g over a period of 15 s. Tensile strength was measured using a tensile tester (MTS Insight 10) under a maximum force of 10 kN at a loading rate of 0.5 mm/min. The tensile force was recorded instantly and estimated at a delay of 0.05% with the set load rate.

$$\text{Scanning volume (V)} = w \bullet h \bullet v \bullet t \tag{1}$$

$$\text{Repetition factor } (C) = \frac{(t \bullet v)}{s} \tag{2}$$

$$E = \frac{P}{(w \bullet h \bullet v \bullet t)} \bullet C \tag{3}$$

where w is the scanning spacing or hatch distance; h is the layer thickness; v is the scanning feed rate; t is the duration of exposure; s is the scanning point distance or point distance; P is the laser power.

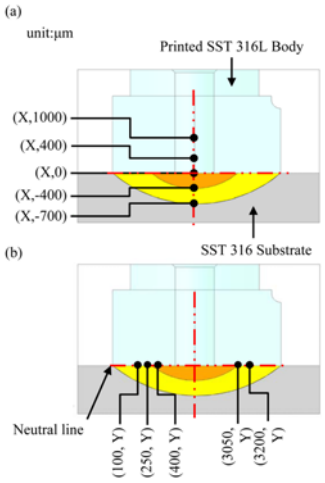

Fig. 2 Schematic illustration showing measurement of microhardness in (a) longitudinal and (b) traverse directions

3. Results and Discussion

3.1 Elemental migration

Figs. 3(a), (b) and (c) illustrate the elemental migration of chrome, molybdenum and nickel elements in the scanned area corresponding to the distance from 300 and 400 μm above and underneath the neutral plane respectively. The migration of chrome, manganese and nickel elements was measured from the layered body (100 μm) into the substrate (-100 μm), ranging from ~18.76% to ~17.39%, ~1.20 to 0.75%, ~11.44 to ~ 9.10% respectively. It was clear that the elemental migrations tended to occur from the high concentration zone to the low zone, but were limited to a few layers only. This was because the high input energy did not produce continuous melting, but only limited penetration underneath the previous molten layers in order to prevent boiling and vaporization before solidification took place. As a result, the heat conduction was constrained by the scanning path which was usually limited in the lateral direction due to each single pass, and kept almost constant in the depth (Z direction) due to the constant coefficient of the thermal conductivity. Thus, the elemental migration activated by the diffusion would be in the same trend as the heat conduction is conveyed. The elemental migration of the nickel and manganese had great mobility since the high atomic mass (Ni: 58.7, Mn: 54.9) and the small elemental scale (Ni: 0.690 Å, Mn: 0.46 Å) could make them very easy to spread and settle into the successive molten pool and alloy the matrix after solidification had occurred. Whereas chromium presented limited effects in the associated dispersion actions. Although the strengthening mechanism in the austenitic stainless was usually produced by strain hardening, the alteration of the elemental migration could also possibly increase the ferrite content in the matrix and produce an austenite-ferrite structure under the equilibrium of stoichiometry and entropy. Thus, the strengthening in the region of the duplex structure could take place.

In the examination of ANOVA, the elemental migration was investigated at the locations 100 μm below and above the neutral plane in order to the observed the progressive alteration in the atomic percentage for the Cr, Mn and Ni elements.

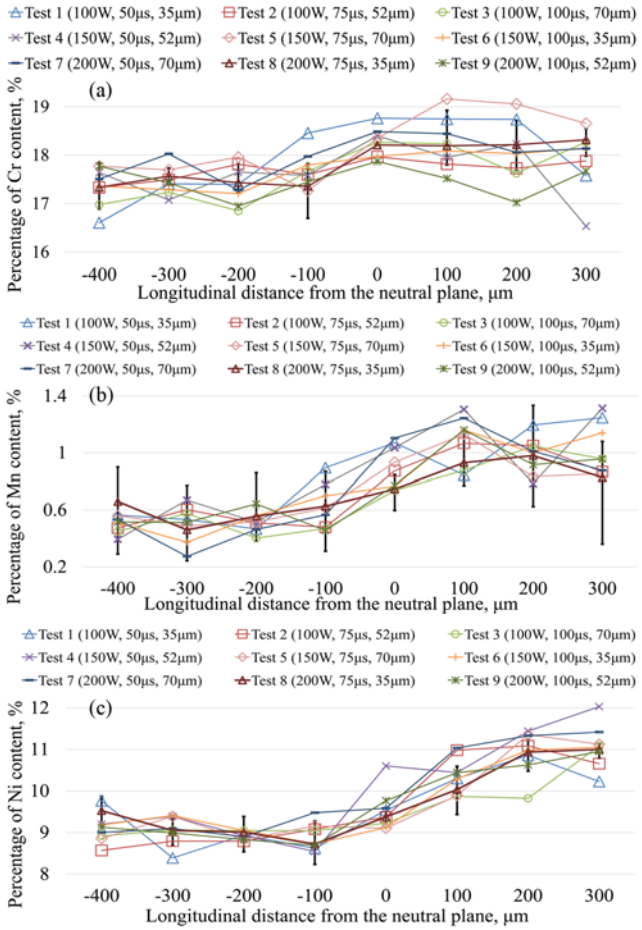

Fig. 3 Elemental migration of (a) chromium (b) manganese (c) nickel elements in the dilution zone

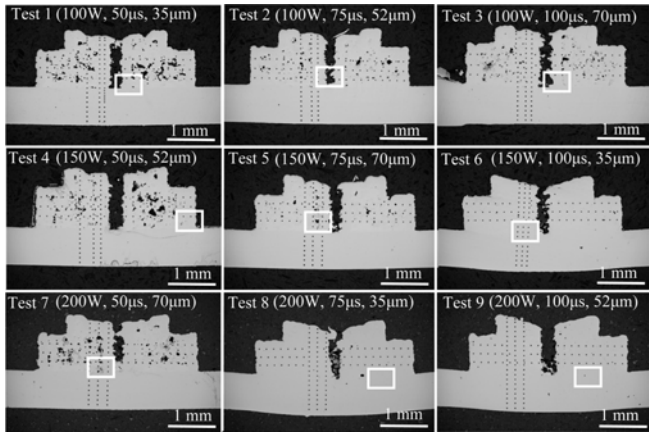

Fig. 4 Micrographs of microhardness indentations on laser- melted stainless steel in longitudinal and traverse directions

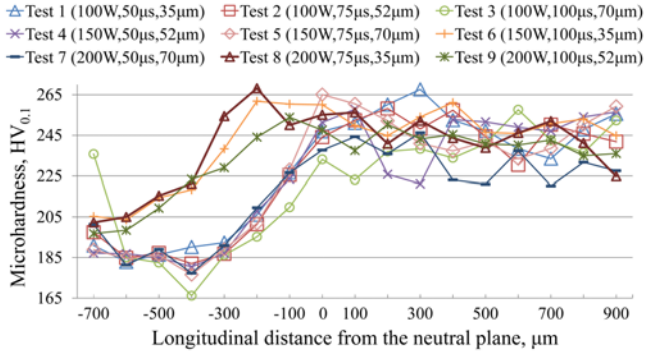

Fig. 5 Measurements of microhardness of layered 316L stainless steel workpieces in the longitudinal direction

3.2 Alteration of microhardness

High hardness is usually required for applications involving heavy duty loads and minimum deflection. The high hardness is achieved by the least mean free path among grains in the matrix, which allows it to withstand plastic deformation. Therefore, hardness can be used as an indicator of the mechanical strength of the matrix. However, microhardness in layer-manufactured materials is different from the hardness required in conventional wrought/cast materials. The former was affected by the formation of secondary phases and superficial changes in the lattice structure from layer to layer, depending on the conditions in the sintering/melting process and the interaction with previous and successive layers. Whereas the latter was usually manipulated by the precipitation of secondary phases in the lattice structure via heat treatment actions.

Fig. 4 presents measured locations for microhardness in the longitudinal (Z-axis) and traverse directions in the specimens. In Fig. 5, the results are presented in two sections. The results on the left are distributed in slopes ramping from ~235.8 to ~268.1 $HV_{0.1}$, corresponding to the interval from the substrate to the neutral plane (interface between the substrate and layered body). The results on the right range from ~265 to 264.5 $HV_{0.1}$, corresponding to the interval from the neutral plane to the upper mask surface. The microhardness results on the left increase incrementally, probably due to the activated elemental migration in the dilution zone; wherein the particles release elements into the matrix of the substrate via diffusion, thereby increasing the amount of nickel in the dilution zone. Thus, the alloying composition in the stainless substrate (SST316) results in the formation of a duplex microstructure, comprising a higher percentage of ferrite in the austenitic matrix, which limits the movement of the matrix and thereby strengthens it. The high microhardness measured in Tests 6, 8, and 9 (~268.1 $HV_{0.1}$) was the coupled results of high input energy densities, i.e. high laser power (150-200 W), long exposure (75-100 μs) and the least point distance (35-52 μm). This assessment is in line with the results from ANOVA. In comparison with the threshold of statistical significance ($F_{0.05\ 2,8}$: 4.64), the operated laser power was significant (F_{cal}: 6.03, PCR of 47.9%). This meant the laser power governed the effect of the dilution by means of increasing the microhardness in the matrix. In contrast, both the exposure and point distance appear to have made limited contributions (PCRs: 8.8% and 5.1%, respectively). Possibly the high energy density in Tests 6, 8, and 9 resulted in the hardening effect in the annealed stainless steel 316L substrates. This was most likely caused by the increase of ferrite content due to the activated diffusion of the fine dispersed elements in the dilution zone. Conversely, insufficient thermal energy in Test 3 (low laser power, short exposure, and larger point distance) limited the amount of heat input to the molten pool, thereby limiting dilution. This,

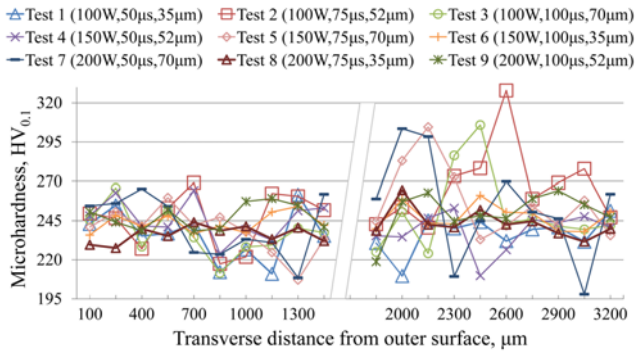

Fig. 6 Measurements of microhardness of layered 316L stainless steel workpieces in the transverse direction

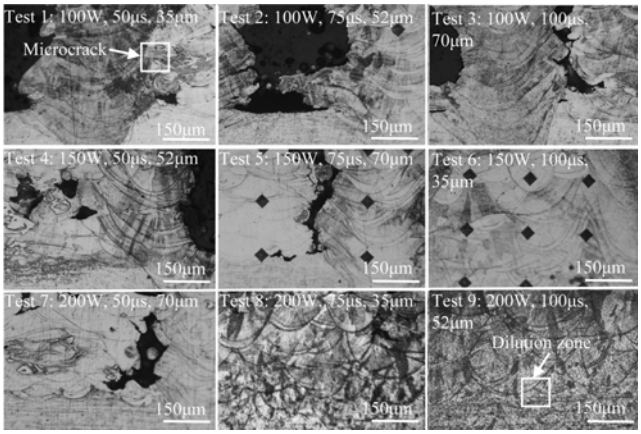

Fig. 7 Microstructures observed in laser-melted 316L stainless steel powder

in turn, constrained age hardening. This decreased solid solubility of the alloying elements caused the matrix to gain limited chromium and nickel, leading to a reduction of the ferrite phase content and limited hardening.

The microhardness results on the right side of the plots present homogeneous distribution, indicating a mean value of 243.8 $HV_{0.1}$ with standard deviation of 18.09 $HV_{0.1}$. However, ANOVA failed to identify any operating variables with a significant effect on microhardness. This is to be expected, due to the fact that the concentrations of nickel and chromium were saturated in the same layer. In addition, the solidification occurred locally in the melting pool which limited the diffusion in the same layer. The new layers also began as a new surface, such that residual heat from previous layers had little influence on successive layers, except in the rare instances where they overlapped along the same scanning paths. With such a short exposure (~100 μs) and rapid scanning speed (220 mm/s), the heat cannot be stored the way it is in casting or powder metallurgy. As a result, thermal softening can essentially be disregarded.

The results of surface microhardness measured across the sectioned plane in the transverse direction presented greater uniformity than those taken from longitudinal sections. As shown in Fig. 6, the average microhardness measurements ranged from 236.2 to 256.5 HV0.1 (mean 245.4 HV0.1) with standard deviation of 5.86. Test 2 revealed a sudden increase in microhardness at 327.9 HV0.1 at a distance of 2600 μm from the outer surface, indicating the location of local hardening. The content of chromium and nickel fell within the specifications of 316L stainless steel, i.e. 17.68% and 11.05%, respectively, meaning none of elemental migration occurred across each scanning pass. None of the operating parameters appeared to be significant in ANOVA or the main effect plots. Obviously, this could be attributed to metallurgical saturation and the stoichiometric equilibrium of the elements in the alloys, which would limit the diffusion or migration of strengthening elements.

Notably the microhardness plot in the transverse direction could differentiate the alloying effects from the continuity of density. In Fig. 6, the measured average microhardness in Tests 2, 3 and 5 had low density values (Test 2: 6.49 g/cm^3, Test 3: 7.19 g/cm^3 and Test 5: 7.04 g/cm^3), but they presented high microhardness values (Test 2: 256.45 $HV_{0.1}$, Test 3: 243.80 $HV_{0.1}$ and Test 5: 247.74 $HV_{0.1}$) sporadically. When the elemental migration had successfully taken place, it increased the microhardness in the matrix, despite the laser heat not being high enough to transfer the matrix into a complete liquid phase and solidify with the high density.

3.3 Microstructure

The microstructures of interest include the fusion zone, the penetration zone beneath the neutral plane, and the phase transformation influenced by thermal energy in the layered bodies (SST 316L powder alloy) and on the substrate (SST316). Fig. 7 shows the microstructures produced from the laser melting of 316L stainless steel powder under various laser power values (100-200 W), exposure durations (50-100 μs) and point distances (35-70 μm) in a Taguchi L_9 array. The specific microstructures (denoted by boxes in Fig. 4) were captured under magnification 2000× to observe the phase transformation and details of the microstructure. Stainless steel is strengthened by the ferrite content in the austenitic matrix and therefore is generally not hardened by heat treatment. In the work done by Abel et al. (1990), they suggested that in wrought 316L stainless steel, the ferrite content was mainly influenced by proportions of nickel (1-10%), chromium (10-20%) and carbon (<0.3%). Therefore, precipitations for the local hardening in the microstructure were not expected in this selective laser melting process either. However, the diffusion of some alloyed elements into the substrate was expected; this would likely increase the percentage of ferrite content. Knowing that the diffusion action was being influenced by the surface energy, interacting with the molten powders, substrate, and the melting pool practically when the laser was set at a low power level of 100 W, the relatively low input heat was not effectively transferred into the molten pool or adjacent areas, resulting in the suppression of the diffusion. As seen in the result of Test 1 from Fig. 7, it shows that the spontaneous adhesion between the layers involved very little penetration due to insufficient input heat which resulted in partial melting. Similar results were observed in Tests 2 and 3. When the established molten pools in the layers were unable to maintain a balance of surface tension amongst the vapour-liquid, liquid-solid and solid-vapour interfaces, very limited penetration of the molten SST 316L powder immersing or spreading into the SST 316 substrate was achieved. In contrast, the imbalance in surface tension caused by partial melting resulted in irregular pores and cracks. The irregular pores were possibly produced due to incomplete consolidation or dislodgement of

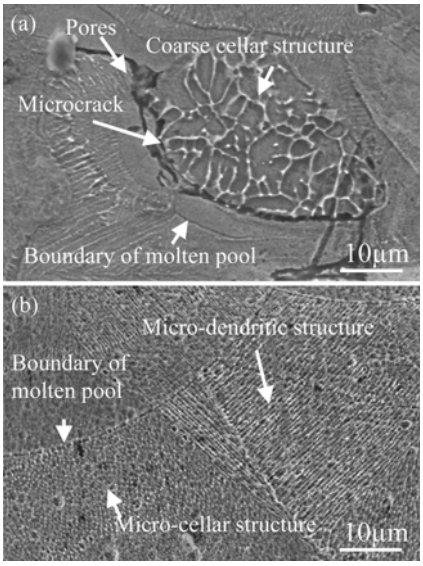

Fig. 8 Microstructures in 316L duplex stainless steel: (a) coarse cellar structure in Test 1 and (b) dendrites in Test 9

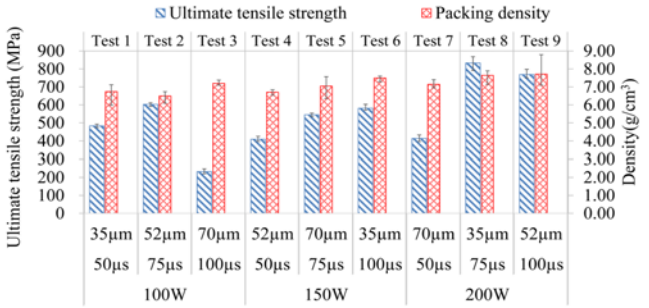

Fig. 9 Correlation between ultimate tensile strength of laser melted 316L stainless steel and material density

powder grains by mechanical forces in the powder-bedding process. This effect was exacerbated after layering in the successive passes, which was seen as cracking, possibly induced by shrinkage in the over-heated zone next to the pores, due to the isolation of the localized heat transfer. However, when the laser power was increased to 200 W, the microstructures underwent broad spreading resulting from complete melting and solidification, and very limited cracks were observed. This was particularly evident in Tests 6, 8, and 9 in which the molten pools extended to ~180 μm in width ~150 μm in depth, which indicates a good balance between heat absorption and heat transfer. This greatly reduced the formation of cracks and pores near to the neutral plane and in the layered body.

Fig. 8 shows the microstructures produced by the extreme conditions under the low and high input energy densities of 761,905 and 10,525,641 W/mm^3 in Tests 1 and 9 respectively. When the preferable combination of parameters employed was the laser power (200 W), exposure (100 μs) and point distance (52 μm) in Test 9, the continuous immersion/dilution actions in the successive layer were activated and the continuous fusion actions would be expected. In Fig 8(b), the microstructures in the dilution zones of the layered body presented an entirely austenitic matrix with a clear boundary of a molten pool, which was produced by the fusion action and characterised with the scale shapes. The micro-dendritic and the micro-cellar structures indicating the results of the ferrite enhancement after the powder particles transformed entirely into a liquid phase in the melting pools and attracted adjacent particles. This led to continuous strengthening followed by local solidification. The availability of heat also appears to have caused the micro-dendrites in the matrix to penetrate into underlying layers in the dilution zone. In contrast, Fig. 8(a) shows the cracks near the boundary in the molten pool as well as a scattering of the coarse cellar structures in the microstructure, which was captured in Test 1. This was due to the insufficient energy input which hindered the elemental migration and did not activate the ferrite enhancement in the microstructure when using low laser power (100-150 W). The powder particles did not become entirely molten, which led to a mixture of liquid-solid in the molten pool.[12] This two-phase mixture reduced the overall rheological performance of the molten liquid pool with regard to the absorption of adjacent solid particles, which become a barrier for the actions of immersing, spreading. Finally, the consolidation ended up with a discontinuous microstructure and did not have a strengthened structure.

3.4 Confirmation test

Generally, the degradation of tensile strength begins with crack initiation and propagation, and ends with fracture in the wrought and cast materials. However, these are not entirely in line with the results produced by laser melting in the layer manufacturing, which could vary with the elemental migration, microstructure, and alteration in the microhardness, particularly when bonding to a heterogeneous material substrate in this study.

Fig. 9 lists the ultimate tensile strength (UTS) results of laser melting stainless steel 316L samples with the associated material density values. The UTS values (232.3-834.0 MPa) were obtained using destructive tensile tests; whereas the material density (6.50-7.71 g/cm^3) was determined by converting the relative density of 81.3-96.4%. Test 3 (laser power of 200 W, exposure of 75 μs, and point distance of 35 μm) resulted in a relatively low UTS of 232.2 MPa and material density of 7.20 g/cm^3, which reflected a conversion ratio of 34.0% compared to the theoretical value of 683 MPa. With the exception of Tests 3, 4, and 7, the ultimate tensile strength values were generally proportional to the material density. This phenomenon was due to the fact that the low density reflected the discontinuity in the matrix and could not transit the load; instead of the massive deflection and deformation at a high strain rate, with limited strain hardening observed before fracture occurred.

In contrast, the workpieces with the low-density values (Tests 2 and 5) could have high strength. This phenomenon was previously confirmed by the elemental migration into the melting pool which strengthened the matrix. Therefore, the ultimate tensile strength was not solely dominated by the density, but significantly influenced by those operating parameters which could effectively develop the elemental migration and simultaneously produce the high density in the workpieces. Similarly, Test 8 (200 W, 75 μs, and 35 μm) resulted in a relatively high UTS of 834.0 MPa with corresponding material density of 7.64 g/cm^3. This satisfactory result of UTS can be attributed to the superior laser melting condition produced by the operating parameters. Aside to the reduced

formation of pores, voids and microcracks in the solidified molten pool, the resulting consolidation process was additionally performed with the smoothened elemental migration of chromium and nickel, a strengthened matrix in the duplex structure, and enhanced microhardness in the neutral place and beneath the substrate up to -700 μm.

4. Conclusions

Based on the results and discussion in the previous sections, the influences of the operating parameters on the elemental migration and the associated alterations of the microhardness and microstructure have been resolved, as well as the improved mechanical performance being confirmed. The migration of chrome, manganese and nickel from the layered body (100 μm) into the substrate (-100 μm) ranged from ~18.76 to ~17.39%, ~1.20 to 0.75%, ~11.44 to ~9.10% respectively. The alteration of the elemental migration could also possibly produce an austenite-ferrite duplex structure and thus strengthening in the region occurred. Moreover, increasing the laser power to 200 W resulted in greater spreading in width (~180 μm) and depth (~150 μm) due to complete melting when using the laser power (200 W), exposure (100 μs), and point distance (52 μm). This combination enabled continuous immersion/dilution in successive layers, resulting in continuous fusion, as indicated by the scale-shaped structures and complete absence of a heat-affected zone, but the presence of micro-dendrites in the matrix. As a result, the high microhardness of the stainless steel workpieces (~268 $HV_{0.1}$), measured in the longitudinal direction, was associated with higher input energy densities. Laser power was shown to be particularly significant (F_{cal}: 6.03, PCR: 47.9%). The hardening effect encountered in annealed 316L stainless steel substrates along the neutral plane was initiated by an increase in ferrite content, which was balanced with the diffusion of finely dispersed elements in the dilution zone. In contrast, microhardness measurements in the transverse direction ranged from 236.2 $HV_{0.1}$ to 256.5 $HV_{0.1}$; however, none of the operating parameters appear to be significant. The contents of chromium and nickel were almost constant and met the specifications of 316L stainless steel, i.e. 17.68% and 11.05%, meaning none of elemental migration occurred across each scanning pass. Under high laser power (200 W), short exposure (75 μs), and small point distance (35 μm), the stainless steel workpieces presented the relatively high ultimate tensile strength of 834.0 MPa (22.1% higher) than the theoretical value (683 MPa) in cast stainless steel. This was due to the fact that a consolidation process was performed with the smoothened elemental migration of chrome and nickel, the strengthened matrix in the duplex structure, and the enhanced microhardness in the neutral place and the substrate.

ACKNOWLEDGEMENT

The authors would like to thank Pegatron Co. Ltd. for providing financial support. We also express our gratitude to the students in the Advanced Manufacturing Research Lab of National Taiwan University of Science and Technology for their assistance.

REFERENCES

1. Wohlers, T. T. and Caffrey, T., "Wohlers Report 2014: 3D Printing and Additive Manufacturing State of the Industry Annual Worldwide Progress Report," Wohlers Associates, 2014.
2. Spackman, C. C., Picha, K. C., Gross, G. J., Nowak, J. F., Smith, P. J., et al., "A Novel Multimaterial Additive Manufacturing Technique for Fabricating Laminated Polymer Nanocomposite Structures," Journal of Micro and Nano-Manufacturing, Vol. 3, No. 1, Paper No. 011008, 2015.
3. Singh, R. and Garg, H. K., "Fused Deposition Modeling – A State of Art Review and Future Applications," Reference Module in Materials Science and Materials Engineering, 2016.
4. Preston, Z., Nickels, L., Capus, J., and Brooks., "3D Printing of Plastic and Titanium Parts for Racing Bicycles," Metal Powder Report, Vol. 68, No. 5, pp. 30-32, 2013.
5. Preston, Z., Nickels, L., Capus, J., and Brooks., "Contract for Testing AM Aerospace Parts Extended," Metal Powder Report, Vol. 69, No. 1, Paper No. 42, 2014.
6. Greul, M., Petzold, F., Greulich, M., and Wunder, J., "Rapid Prototyping Moves on Metal Powders," Metal Powder Report, vol. 52, No. 10, pp. 24-27, 1997.
7. Das, S., "Physical Aspects of Process Control in Selective Laser Sintering of Metals," Advanced Engineering Materials, Vol. 5, No. 10, pp. 701-711, 2003.
8. Fischer, P., Romano, V., Weber, H.-P., Karapatis, N., Boillat, E., and Glardon, R., "Sintering of Commercially Pure Titanium Powder with a Nd: YAG Laser Source," Acta Materialia, Vol. 51, No. 6, pp. 1651-1662, 2003.
9. Rombouts, M., Kruth, J.-P., Froyen, L., and Mercelis, P., "Fundamentals of Selective Laser Melting of Alloyed Steel Powders," CIRP Annals-Manufacturing Technology, Vol. 55, No. 1, pp. 187-192, 2006.
10. Kruth, J.-P., Froyen, L., Rombouts, M., Van Vaerenbergh, J., and Mercells, P., "New Ferro Powder for Selective Laser Sintering of Dense Parts," CIRP Annals-Manufacturing Technology, Vol. 52, No. 1, pp. 139-142, 2003.
11. Gu, D. and Shen, Y., "Balling Phenomena During Direct Laser Sintering of Multi-Component Cu-Based Metal Powder," Journal of Alloys and Compounds, Vol. 432, Nos. 1-2, pp. 163-166, 2007.
12. Čapek, J., Machová, M., Fousová, M., Kubásek, J., Vojtěch, D., et al., "Highly Porous, Low Elastic Modulus 316L Stainless Steel Scaffold Prepared by Selective Laser Melting," Materials Science and Engineering: C, Vol. 69, pp. 631-639, 2016.
13. Khademzadeh, S., Parvin, N., and Bariani, P. F., "Production of NiTi Alloy by Direct Metal Deposition of Mechanically Alloyed Powder Mixtures," Int. J. Precis. Eng. Manuf., Vol. 16, No. 11, pp. 2333-2338, 2015.

14. Tolosa, I., Garciandía, F., Zubiri, F., Zapirain, F., and Esnaola, A., "Study of Mechanical Properties of AISI 316 Stainless Steel Processed by "Selective Laser Melting", Following Different Manufacturing Strategies," The International Journal of Advanced Manufacturing Technology, Vol. 51, Nos. 5-8, pp. 639-647, 2010.

15. Choi, S.-H., Sohn, I.-B., and Lee, H., "Femtosecond Laser-Induced Line Structuring on Mold Stainless Steel STAVAX with Various Scanning Speeds and Two Polarization Configurations," Int. J. Precis. Eng. Manuf., Vol. 13, No. 6, pp. 845-854, 2012.

16. Wei, Q., Li, S., Han, C., Li, W., Cheng, L., et al., "Selective Laser Melting of Stainless-Steel/Nano-Hydroxyapatite Composites for Medical Applications: Microstructure, Element Distribution, Crack and Mechanical Properties," Journal of Materials Processing Technology, Vol. 222, pp. 444-453, 2015.

17. Sun, Z., Tan, X., Tor, S. B., and Yeong, W. Y., "Selective Laser Melting of Stainless Steel 316L with Low Porosity and High Build Rates," Materials & Design, Vol. 104, pp. 197-204, 2016.

18. Hao, L., Dadbakhsh, S., Seaman, O., and Felstead, M., "Selective Laser Melting of a Stainless Steel and Hydroxyapatite Composite for Load-Bearing Implant Development," Journal of Materials Processing Technology, Vol. 209, No. 17, pp. 5793-5801, 2009.

19. AlMangour, B., Grzesiak, D., and Yang, J.-M., "Rapid Fabrication of Bulk-Form TiB2/316L Stainless Steel Nanocomposites with Novel Reinforcement Architecture and Improved Performance by Selective Laser Melting," Journal of Alloys and Compounds, Vol. 680, pp. 480-493, 2016.

20. Joo, S.-M., Bang, H.-S., and Kwak, S.-Y., "Optimization of Hybrid CO2 Laser-GMA Welding Parameters on Dissimilar Materials AH32/ STS304L Using Grey-Based Taguchi Analysis," Int. J. Precis. Eng. Manuf., Vol. 15, No. 3, pp. 447-454, 2014.

21. Chen, H., Gu, D., Dai, D., Ma, C., and Xia, M., "Microstructure and Composition Homogeneity, Tensile Property, and Underlying Thermal Physical Mechanism of Selective Laser Melting Tool Steel Parts," Materials Science and Engineering: A, Vol. 682, pp. 279-289, 2017.

22. Zhu, Y., Zou, J., Chen, X., and Yang, H., "Tribology of Selective Laser Melting Processed Parts: Stainless Steel 316L under Lubricated Conditions," Wear, Vols. 350-351, pp. 46-55, 2016.

23. Sander, G., Thomas, S., Cruz, V., Jurg, M., Birbilis, N., et al., "On the Corrosion and Metastable Pitting Characteristics of 316L Stainless Steel Produced by Selective Laser Melting," Journal of the Electrochemical Society, Vol. 164, No. 6, pp. C250-C257, 2017.

24. Suryawanshi, J., Prashanth, K., and Ramamurty, U., "Mechanical Behavior of Selective Laser Melted 316L Stainless Steel," Materials Science and Engineering: A, Vol. 696, pp. 113-121, 2017.

25. Cherry, J., Davies, H., Mehmood, S., Lavery, N., Brown, S., and Sienz, J., "Investigation into the Effect of Process Parameters on Microstructural and physical Properties of 316L Stainless Steel Parts by Selective Laser Melting," The International Journal of Advanced Manufacturing Technology, Vol. 76, Nos. 5-8, pp. 869-879, 2015.

26. Wang, Z., Palmer, T. A., and Beese, A. M., "Effect of Processing Parameters on Microstructure and Tensile Properties of Austenitic Stainless Steel 304L Made by Directed Energy Deposition Additive Manufacturing," Acta Materialia, Vol. 110, pp. 226-235, 2016.